Powerline Perching with a Fixed-Wing UAV

Joseph Moore [*] and Russ Tedrake [†]

MIT Computer Science and Artificial Intelligence Lab, Cambridge, MA, 02139, USA

The ability to land on a powerline to recharge will dramatically enhance the endurance and therefore mission capabilities for small UAVs. The magnetic fields around these powerlines have a well known structure. In this paper we evaluate the possibility of using onboard magnetometers, in combination with an inertial measurement unit and dynamic model of the aircraft, to localize the vehicle relative to the powerline. Specifically, we investigate the near-field structure of a dipole magnetic field configuration and demonstrate that state estimation using particle filters can provide sufficiently accurate, high-bandwidth, and low-latency estimates to be compatible with aggressive near-field maneuvering by the aircraft to acquire to perch on the line.

Nomenclature

j	imaginary number
ω	angular frequency
t	time
c	carrier signal
m	message signal
v	modulated message signal
V	frequency domain modulated message signal
N	frequency domain message signal
W	signal immediately after demodulation
π	3.14159...
δ	dirac delta function
j	imaginary number
ω	angular frequency
$\vec{B}$	magnetic field vector
I_c	current
B_x	magnetic field component in x-direction
B_z	magnetic field component in z-direction
μ_0	permeability of air
d	distance between wires
x	position along the x-axis
z	position along the z-axis
p	probability
$\overline{bel}$	belief prediction
η	normalization constant
i	an individual particle
N_s	number of particles
$\dot{x}_k$	x-velocity at discrete step k
$\dot{z}_k$	z-velocity at discrete step k
$\dot{\theta}_k$	pitch at discrete step k
ϕ_k	elevator angle at discrete step k

---

[*] PhD Candidate, Department of Mechanical Engineering, AIAA Student Member.

[†] Associate Professor, Department of Electrical Engineering and Computer Science, AIAA Member.

$\dot{\phi}_k$	angular velocity of elevator
x_k	x-position at discrete step k
z_k	z-position at discrete step k
θ_k	pitch at discrete step k
$\dot{x}_w$	wing velocity along x-direction
$\dot{z}_w$	wing velocity along z-direction
$\dot{x}_e$	elevator velocity along x-direction
$\dot{z}_e$	wing velocity along z-direction
α_w	wing angle of attack
α_e	elevator angle of attack
F_w	aerodynamic force perpendicular to the wing
F_e	aerodynamic force perpendicular to the elevator
S_w	wing area
S_e	elevator area
l_e	elevator length (measured from the center of the elevator)
l	distance from back of fuselage to the center of mass
l_w	distance from center of the wing to the center of mass
Δt	discrete time step
g	acceleration of gravity
w_k	particle weights at discrete step k
σ	standard deviation
I	inertia

I. Introduction

Small and micro UAVs have enabled a number of new mission capabilities, including navigating in and around buildings and performing perch-and-stare surviellance. However, one of the primary limitations in these small vehicles is endurance, simply because they cannot carry sufficient power for long missions. Recent advances in fixed-wing perching[1–4] have made it possible to consider a new solution to this problem - landing on a powerline to recharge. In order to pursue this vision, we have teamed with the AFRL's Power-Line Urban Sentry (PLUS) team, who have already demonstrated recharge capabilities using a portable inductive power coupling.

II. Why use magnetic field localization?

With the rise of camera-based vision systems in robotics, one must ask the question why magnetic field localization is the best method of locating a powerline. Even if sufficient computational resources are available onboard, even locating a powerline can be a daunting task for computer vision in visually cluttered environments. Furthermore, it may be complicated to accurately estimate the distance to the powerline which may appear as only a few pixels in an onboard camera. Thus, because the magnetic beacons are already provided by powerlines and because the structures are fairly well known, magnetic field localization seems to emerge as the best solution. Furthermore, magnetic field sensing approaches are typically less computationally intensive as well as lest costly when compared to camera-based vision approaches.

III. Related Work

In the past a great deal of research has gone into state estimation, especially in the aerospace community. For many, the Kalman Filter exists as the major milestone in estimation techniques, and has certainly been used in numerous applications to predict the location of a wide variety of bodies in flight. Similarly, the area of magnetic field sensing and measurement is also fairly well researched and understood. Often involving the Kalman Filter, much research effort has gone into using the earth's magnetic fields to determine the orientation of an aircraft. One of the more unique applications of magnetic sensors in the aerospace field has been the use of magnetic dipoles to achieve collision avoidance within a group of UAVs through total field sensing.[5] By far, however, the related work having the greatest relevance to this project is the work done the sponsor, the Defense Research Associates, as well as the Robot Locomotion Group iteslf. For the past several years, the DRA has been working in conjunction with the Airforce Research Laboratory to achieve power harvesting from electric lines with small UAVs.[6] The Power Line Urban Sentry (PLUS) program which they began has achieved impressive results in both inductive coupling as well as powerline magnetic field modeling and characterization. At MIT, the Robot Locomotion Group has been working in parallel to develop advance perching control algorithms[1,7] and system identification techniques[8] to aide in these power harvesting tasks. The state estimation project outlined in this paper is meant to bring all these different subtasks together, with the hopes of eventually developing an autonomous perching and power harvesting UAV.

IV. Objective and Experimental Approach

The objective of this project was to develop a method of accurately estimating the states of a fixed wing aircraft as it approaches a powerline on a perching trajectory, using only an on-board combination of magnetic and inertial sensor measurements. Because both the perching trajectory and the magnetic field structure are primarily isolated to a single plane in space, it was also decided that the system dynamics could be more simply represented in two dimensions for the purposes this initial investigation. Early on, it was determined that the magnetic sensors would be used to obtain the positions and velocities of the aircraft's center of mass, while measurements from inertial sensors would provide the aircraft's orientation and angular rates, and it has been this concept which has guided much of the design process so far.

V. Indoor Powerline Experimental Set-Up

The very first step in achieving the localization of a fixed-wing aircraft in the presence of the magnetic field generated by a high-current carrying wire was to develop an electrical system capable of simulating the conditions that might be found around a real, outdoor powerline. Thus, it becomes important to investigate what type of magnetic field structure is found in the real-world outdoor environment. In the standard, three phase electrical systems found in many power delivery networks, three wires carry three currents, all of which are 120 degrees out of phase with one another. In this case, if all three wires occupied the same space, the resulting magnetic field would sum to zero. However, because there is a small space between the wires, a resulting magnetic field, forms around the wire. Interestingly, because of the zero net current condition, the magnetic field that arises around a powerline possesses a similar structure to that of the more familiar dipole magnetic field. Thus, instead of adopting the complexity which may be associated with implementing a three phase system, a two phase system with a similar field structure was selected instead.

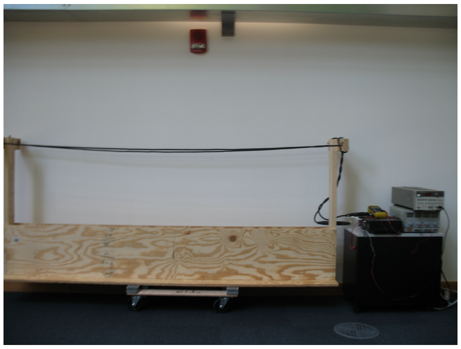

Figure 1. Photo of Powerline Perch

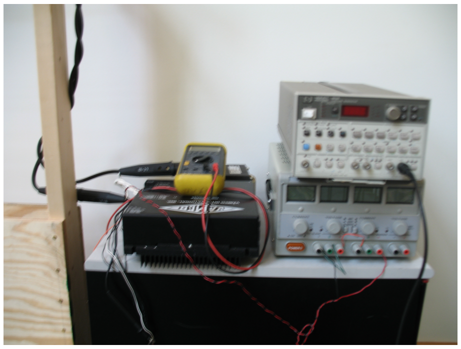

Figure 2. Close up of Power Electronics

To implement the two phase system, a 4 gage welding wire was selected to carry a current near 40 amps. This level of current was selected because it would provide just about four times the minimum field strength capable of being picked up by the magnetic sensors (40 uV). It was also reasoned, that because of the surrounding 60 Hz noise often found in indoor environments, it would be beneficial to be able to vary the frequency of the wire's current to avoid interference. To achieve this functionality, a PWM current controller DC Motor amplifier from Advanced Motion Devices capable of carrying out sinusoidal commutation and generating currents around 50 Amps peak-to-peak, was connected in series with a twelve foot loop of 4 gage

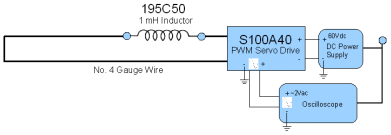

Figure 3. Block Diagram of Powerline Set-up

wire and a 1 mH inductive load. The motor amplifier was then fed by 600 watt DC power supply and driven by a conventional oscilloscope capable of adjusting the frequency, amplitude, and offset of the current. To create the dipole configuration, a wooden stand was built to orient the rectangular loop of wire, 2.4 meters long by 0.3 meters wide in a Vicon Motion Capture Environment, so as to provide dead-reckoning for the experiments.

VI. Signal Pick-up Methodology

Because the currents flowing through conventional power lines are alternating in nature with an unknown phase, one has two choices with regard to obtaining the vectors of a magnetic field at a given position in space, both of which emerge out of conventional amplitude demodulation techniques used in many electromagnetic receivers. The first choice is known as envelope detection, or asynchronous detection. By far the simpler method, envelope detection obtains the values of the peaks of a modulating signal, bandpassed at the desired frequency. In analog circuitry, this method requires incoming signal to be rectified via a diode and lowpass filtered so as to obtain the envelope of the signal. The same can also be done in software by creating a moving window which takes the maximum value of the incoming peaks. There are, however, several disadvantages to using this method. Envelope detectors often exhibit distortion, especially when the carrier frequency is not strong enough, and they also perform poorly with respect to noise when the signal values are low.

The second choice, and the preferred method of this paper, is synchronous demodulation. In this method, after the signal is bandpass filtered at the frequency of choice, it is multiplied by a local oscillator having the same frequency and phase as the incoming signal. This forces the band-limited signal to be centered around the origin instead of being centered around the original frequency of modulation. The resulting signal can then be low passed filtered to remove the higher frequency noise injected into the signal during the demodulation process.

The Derivation Below Corresponds to the Frequency Domain Representation of Amplitude Demodulation as represented in figures 4 and 5.

The carrier frequency is given by $c(t)$ which, in our case, is 80 Hz.

$$c(t) = e^{j\omega_c t} \tag{1}$$

$v(t)$ represents the signal after it is modulated with the carrier. A sinusoidal function with the envelope of the message signal has been created.

$$v(t) = m(t)e^{j\omega_c t} \tag{2}$$

Use the Fourier Transform to transform $v(t)$ into the frequency domain.

$$V(j\omega) = \frac{1}{2\pi} M(j\omega) * \pi(\delta(\omega - \omega_c) + \delta(\omega - \omega_c)) \tag{3}$$

Because the signal $M(j(\omega - \omega_c))$ is being convolved with a delta function at a frequency of 80 Hz, the message signal is shifted by 80 Hz in each direction, and now becomes centered around +/- 80 Hz.

$$V(j\omega) = \frac{1}{2} M(j(\omega - \omega_c)) + \frac{1}{2} M(j(\omega + \omega_c)) \tag{4}$$

Multiply the signal $v(t)$ in the time domain by a sinusoid at the frequency of the carrier. This becomes convolution in the time domain

$$W(j\omega) = \frac{1}{2}(M(j(\omega - \omega_c)) + M(j(\omega + \omega_c))) * \pi(\delta(\omega - \omega_c) + \delta(\omega - \omega_c)) \tag{5}$$

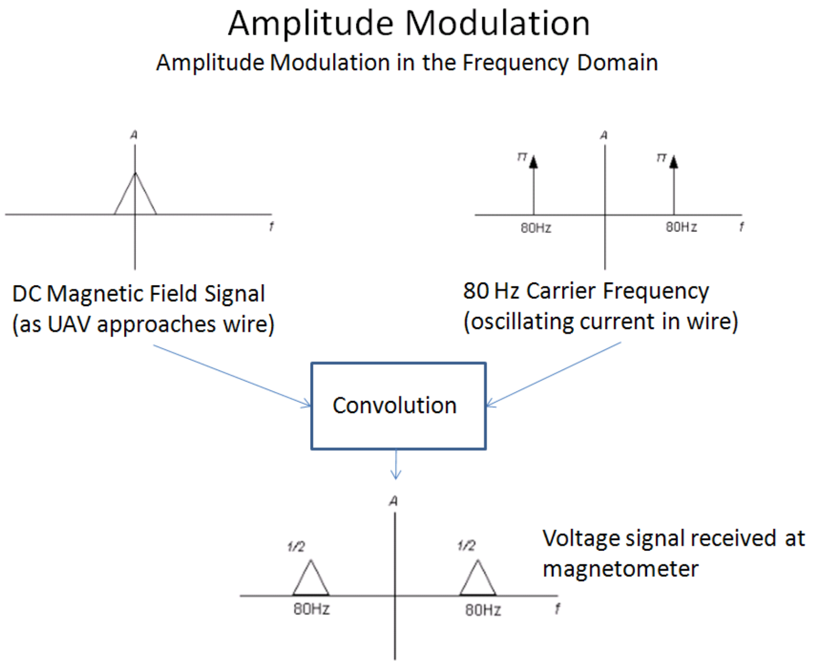

Figure 4. Classical Frequency Domain Representation of Amplitude Modulation

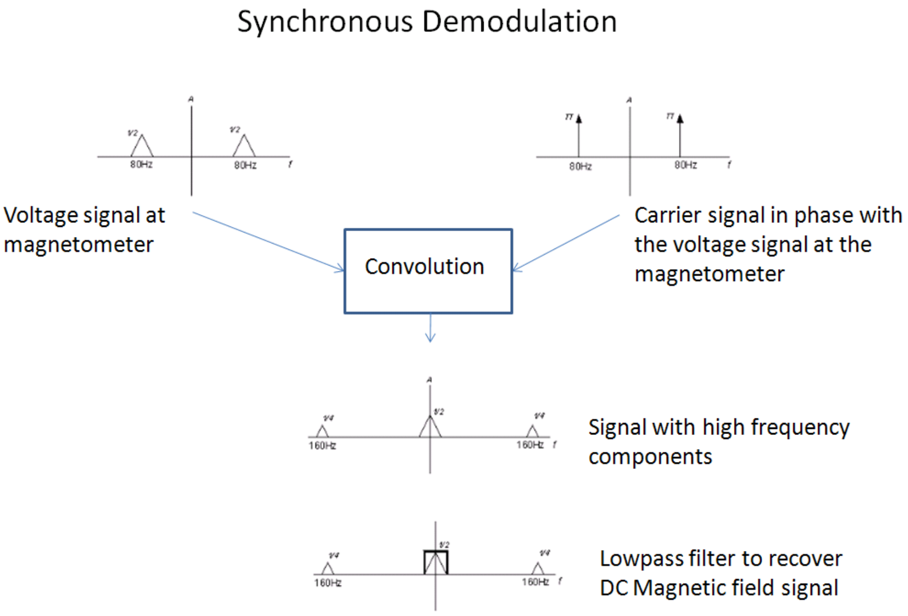

Figure 5. Classical Frequency Domain Representation of Amplitude Demodulation

The delta function causes the message signal to move again, this time to the origin and to +/- 160 Hz. A low pass filter can now be used to remove the high frequency components, leaving the the DC Message signal.

$$W(j\omega) = \frac{1}{2}M(j\omega) + \frac{1}{4}M(j(\omega + 2\omega_c)) + \frac{1}{4}M(j(\omega - 2\omega_c)) \tag{6}$$

See figures 4 and 5 for a visualization of this process.

The major disadvantage of the synchronous detection method is that it is very difficult to obtain an exact representation of the modulating sinusoid (phase and amplitude) at the receiver. In many cases, especially in analog circuit design, a phase-lock loop is used to obtain the local oscillator with the correct magnitude and phase. These phase locked loops are essentially feedback loops which drive the phase of the local oscillator to match that of the incoming waveform. There is, however, another method of obtaining an exact representation of the message signal which does not necessarily require a phase locked loop. This method is know as Complex Synchronous Detection,or Quadrature Demodulation, and is particularly well suited to embedded implementation. It is well known that any sinusoidal signal with a given phase can be decomposed into both a cosine component and sine component. If instead, the incoming signal is multiplied by both a cosine and a sine, and the independent, resulting signals are low pass filtered, these two filtered signals can be squared and summed to reproduce resulting magnitude of the message signal. Fortunately, the complex synchronous demodulation method alleviates many of the disadvantages of envelope detection. There is, however, one disadvantage which plagues both methods, and that is the notion of phase-amplitude ambiguity. Because one never has access to the actual carrier frequency, one can never know whether the incoming signal is out of phase or if the amplitude of the message signal is negative. Homodyne detection does provide a solution to this problem by getting access to the carrier frequency by bandpass filtering extremely close to the nominal carrier frequency. In theory, the resulting band-passed signal should allow the modulated signal to demodulate its self, but in practice, this method still suffers from some robustness issues, making the demodulated signals somewhat unreliable.

Complex Synchronous Demodulation technique:
If

$$y(t) = A(t)cos(2\pi ft + \theta) \tag{7}$$

then one can recover the full signal by multiplying $y(t)$ by $sin(2\pi ft)$ and by $cos(2\pi ft)$. By low-pass filtering these two signals, one is able to produce two signals which are 90 degrees out of phase with one another but, together they represent the real and complex components of the message signal. Thus, by taking the magnitude of these component signals, the true message signal is recovered.

Complex Synchronous Demodulation leaves creates two signals a and b which are equivalent to the message signal, a+bj:

VII. Magnetic Field Model

Without a doubt, the main benefit of using a dipole magnetic field is its well-studied structure in electromagnetic theory. Both its far-field and near field characteristics are well known and documented. When considering a dipole magnetic field it is simplest to think about the field as the superposition of the two oppositely oriented, circular magnetic fields typically found surrounding a long straight wire. By the adding the vector equations for a magnetic field around a long straight wire, one can easily obtain the equations of the x and z coordinates in terms of the magnetic field vector components Bx and Bz.

The equation for the components of a magnetic field around a long straight wire:

$$\vec{\mathbf{B}} = \begin{pmatrix} Bx \\ Bz \end{pmatrix} \tag{8}$$

$$B_z = \frac{\mu_0 I_c x}{2\pi(x^2 + z^2)} \tag{9}$$

$$B_x = -\frac{\mu_0 I_c z}{2\pi(x^2 + z^2)} \tag{10}$$

Using these equations, the dipole equation can be derived through superposition:

$$B_z = -\frac{\mu_0 I_c (x-d)}{2\pi((x-d)^2 + z^2)} + \frac{\mu_0 I_c (x+d)}{2\pi((x+d)^2 + z^2)} \tag{11}$$

$$B_x = \frac{\mu_0 I_c z}{2\pi((x-d)^2+z^2)} - \frac{\mu_0 I_c z}{2\pi((x+d)^2+z^2)} \tag{12}$$

It is important to note that d represents the distance between the wires. These equations can the be used to solve for x and z in terms of B_x and B_z.

The equations result in four pairs of equations for each coordinate, two of which yield imaginary roots, and two of which represent different locations within the magnetic field. Given the direction and magnitude of both the x and y components of the magnetic field, a point could be identified at one of any two points in the magnetic field.

Unfortunately, as discussed previously, the synchronous demodulation algorithm prevents one from knowing the absolute sign of the magnetic field vectors. The best one can achieve is whether or not both the x and z vectors have the same sign or have opposite signs. Therefore, to resolve this phase-amplitude ambiguity, an additional magnetic sensor was added to the aircraft. By knowing the location of two points in space and the orientation of the aircraft, one can resolve this ambiguity.

VIII. Initial Experimental Results

Before the sensing technology was implemented on the fixed-wing UAV, it was first developed separately and tested on a platform which could be moved around in the magnetic field by hand. The test-platform consisted of four pairs of non-inverting amplifiers and corresponding high-pass filters, the magnetometers, and a Labjack data acquisition system. The purpose of the analog circuitry was to eliminate the DC bias of the magnetometers and amplify their AC components appropriately. Several trials were conducted in the presence of a magnetic field oscillating at 10Hz by moving the test-platform through a range of x and z positions and then processing the data offline.

The off-line data processing consisted of bandpass filtering the signal with a second order Butterworth filter at bandwidth of 1Hz. The synchronous demodulation techniques were then carried out, and the equations for the magnetic field were then used to estimate the position of the test-platform from the demodulated magnetic field vectors. To resolve the phase-amplitude ambiguity, all sets of possible coordinates were computed using the given magnetic field vectors, and then the correct points were selected using the known distance between the magnetic sensors and the horizontal orientation of the platform.

IX. On-board Sensing Hardware

Once the initial experimental trials proved the feasibility and potential high-level of accuracy for localizing a body in the magnetic field, hardware development for the on-board sensing equipment commenced. At the core of the sensing hardware exists the ATMEGA128 AVR micro-controller, which is responsible for completing all the analog to digital conversion, low-level control, and signal processing. The micro-controller is also capable of interfacing via serial at 100Hz with the small scale gumstix linux computers for higher-level control applications. X and z accelerations as well as rotation rates about the y-axis are sent to the micro-controller as 0-5 volt voltage levels from the Freescale MMa7260Q accelerometer and the ADXRS300 gyroscope. The analog signals from the HMC2003 three-axis magnetometers are first bandpass filtered with an analog filter having cutoff frequencies at 20Hz and 100 Hz and then passed through a differential amplifier, AMP04EP, and amplified by gain of 20. The magnetometer signals are then sent through a multiplexer to two channels on the micro-controller's analog to digital converter capable of applying variable gains. Because the magnetometer voltage levels increase as $\frac{1}{r^2}$, variable gains are desirable in order to keep the signals from saturating the 5 volt region. To drive the elevator a HS-55 Hitech hobby servo at the center of the glider is controlled via pulse width modulation by the micro-controller. All together, the system runs on a 2 cell 300 maHr Full River Lithium Polymer Cell, and has a total weight of 241 grams.

To examine in-flight data in the presence of the power-line's magnetic field, the micro-controller was programmed to deflect the elevator upon sensing a spike in the acceleration. A cross-bow like launcher featuring a carbon fiber bow was used to launch the glider at the power-line as the aircraft uses its elevator to execute an open loop trajectory. The noise induced by the launch in the electronics signals has caused some difficulty in data processing, and is currently being addressed.

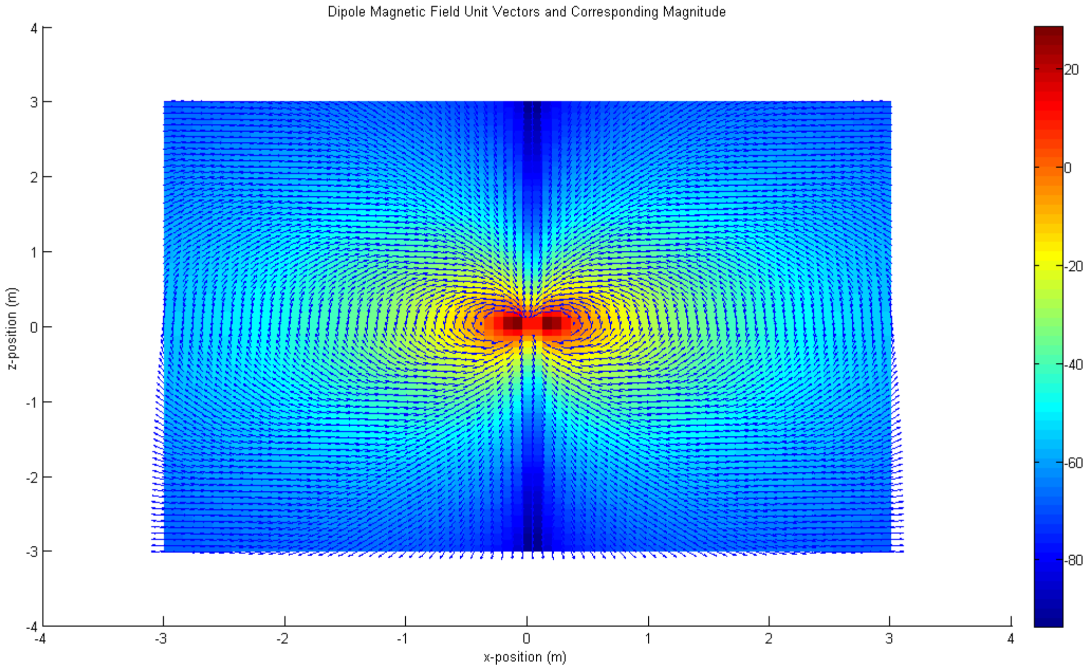

Figure 6. Two Dimensional Plot of Magnetic Field Model

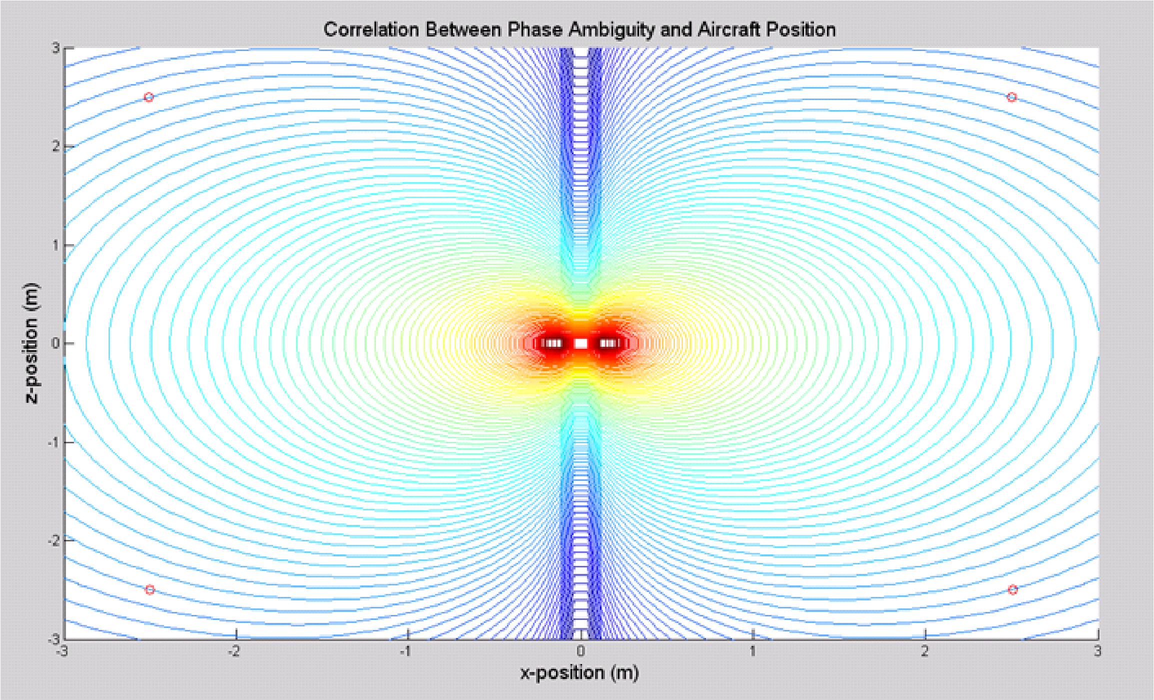

Figure 7. Result of Demodulation Phase Ambiguity

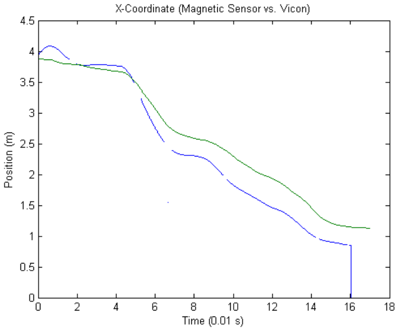

Figure 8. Initial Estimation Results A: x-coordinate

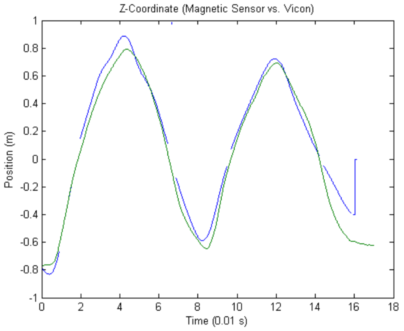

Figure 9. Initial Estimation Results A: z-coordinate

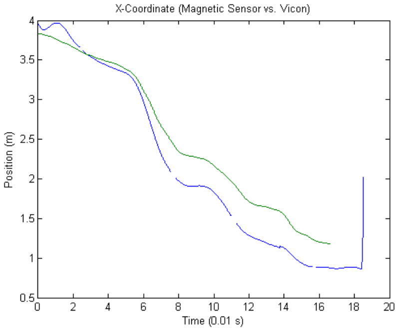

Figure 10. Initial Estimation Results B: x-coordinate

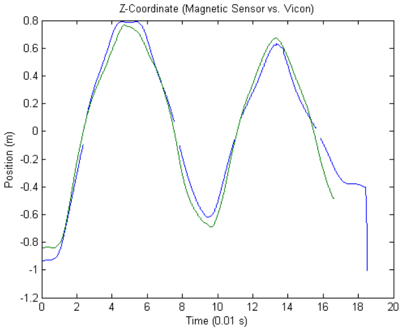

Figure 11. Initial Estimation Results B: z-coordinate

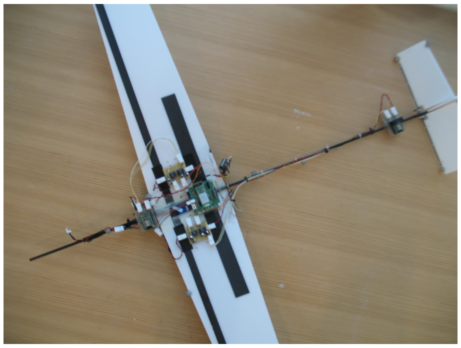

Figure 12. Photo of Instrumented Glider

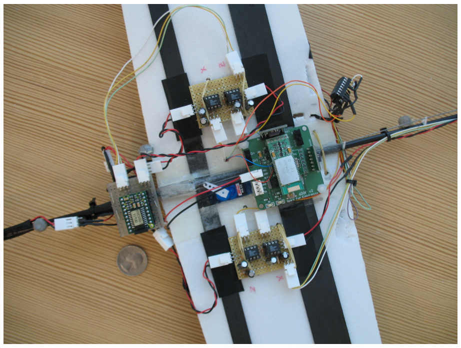

Figure 13. Close-up of Glider Electronics

X. State Estimation via Particle Filter

Recently, with the ever-increasing nature of computational capabilities, Particle Filters have become more and more prevalent as a practical solution for state estimation. These filters, which rely on a collection particles to evaluate a given estimate's probalistic distribution, have the several unique properties. One such property is their ability to cope with nonlinear and multi-modal probability distributions. Another is their ability to handle highly nonlinear models with regards to the process and measurement equations. It is these two properties which make the particle filter the best choice for estimating the state of a glider on a perching trajectory using magnetic field measurements. As previously mentioned, the ambiguity between the phase and amplitude of a magnetometer reading allows for four possible locations if a magnetic field measurement is propagated through equations relating the magnetic field vectors to the x and y coordinates. Because of its ability to manage multi-modal probability distributions, the particle filter, by using the dynamics of the system, is able to reason about these possible locations and determine the most probable estimation for the vehicle's center of mass. Furthermore, because the post-stall dynamics of a perching maneuver are highly nonlinear, the particle filter has a distinct advantage over the Extended Kalman Filter since it does not have to linearize the system equations in order to determine the estimation covariance.

At a fundamental level, particle filters are a method of approximating a recursive Bayesian filter. From the discrete version of Bayes rule we know that the probability of x given the probability of y is equivalent to the probability of y given the probability of x multiplied by the probability of x and divided by the probability of y as shown below:

$$p(x|y) = \frac{p(y|x)p(x)}{p(y)} \tag{13}$$

This law forms the foundation for the Bayes Filter. However, to properly understand the Bayes filter, one must also first understand the notion of belief or bel. A belief can be defined as a conditional probability distribution which takes into consideration all available information at a given point in time, including measurements. This probability distribution is then able to characterize the likely value of a given state. If measurements are not included, the belief is reduced to merely a prediction of the belief, denoted here as $\overline{bel}$. Thus we have established the two main components of most continuous time filters, a probability density corresponding to a prediction, and a probability density corresponding to a measurement. If the belief and its prediction are implemented recursively, one obtains the general form of Bayes filter.

$$\overline{bel}(x_t) = \int p(xt|u_t, x_{t-1})bel(x_{t-1})dx_{t-1} \tag{14}$$

$$bel(x_t) = \eta p(z_t|x_t)\overline{bel}(x_t) \tag{15}$$

From the equations above, one can observe how the current inputs and previous states of a system contribute to the belief's prediction and then how that prediction and an incoming measurement combine to form the actual belief. Without a doubt, the ability to keep track of a state's probability distribution becomes an incredible tool in estimating the states of a system. And yet, there still is one problem - in order to make use of this filter, one must be able to take the integral of the predicted belief. Unfortunately, this can only be done analytically if the distribution is Gaussian, as in the case of the Kalman filter. For other distributions, such as multi-modal distributions, closed form solutions do not exist. Thus one must resort to a more computationally intensive approach by using a collection of particles, chosen by sampling randomly from an approximate distribution, to represent the posterior probability density function in what is known as a particle filter. The algorithm is as follows:

Step 1: Sample x_t^i particles from the distribution $p(x_t|u_t, x_{t-1}^i)$
Step 2: Weight the particles based on the assumed distribution of $p(z_t|x_t)$ and normalize the weights
Step 3: Estimate the current state as the mean of the particles corresponding to that state
Step 4: Re-sample to eliminate samples with low weights.

The re-sampling section of the algorithm merely draws, with replacement, particles from the current set of particles with a probability proportional to the weights of the particles. This newly drawn set of particles then replaces the current set of particles, thus causing the probability density to contract. The weights are then reset to $\frac{1}{N}$.

In the case of the glider, the states were estimated using a model derived through the application of flat-plate theory and system identification from previous investigations. This model was then discretized for the purposes of implementing the particle filter.

The model used was taken from previous Robot Locomotion Group publications and the notation has remained almost entirely consistent with those works. A illustration of the glider model can be seen below.

To compute the glider's forward dynamics, several additional variables have been defined. $\dot{x}_w$ and $\dot{z}_w$ are the wing velocities in the x and z directions respectively. $\dot{x}_e$ and $\dot{z}_e$ are the elevator velocities in the x and z directions respectively. α_w is the angle of attack of the wing, α_e is the angle of attack of the elevator, F_w is the aerodynamic force exerted on the wing, and F_e is the aerodynamic force exerted perpendicular to the elevator. The elevator is assumed to have first order dynamics with the gain K_s. The equations of motion are as follows, and are carried out for every particle:

$$\dot{x}_w = \dot{x}_{k-1} - l_w \dot{\theta}_{k-1} sin(\theta_{k-1}) \tag{16}$$

$$\dot{z}_w = \dot{z}_{k-1} + l_w \dot{\theta}_{k-1} cos(\theta_{k-1}) \tag{17}$$

$$\alpha_w = \theta_{k-1} - \arctan \frac{\dot{z}_w}{\dot{x}_w} \tag{18}$$

$$F_w = \rho S_w sin(\alpha_w)(\dot{z}_w^2 + dotx_w^2) \tag{19}$$

$$\dot{x_e} = \dot{x}_{k-1} + l\dot{\theta}_{k-1}\sin(\theta_{k-1}) + l_e(\dot{\theta}_{k-1} + k_s(u_k - \phi_{k-1}))\sin(\theta_{k-1} + \phi_{k-1}) \tag{20}$$

$$\dot{z_e} = \dot{z}_{k-1} - l\dot{\theta}_{k-1}\cos(\theta_{k-1}) - l_e(\dot{\theta}_{k-1} + k_s(u_k - \phi_{k-1}))\cos(\theta_{k-1} + \phi_{k-1}) \tag{21}$$

$$\alpha_e = \theta_{k-1} + \phi_{k-1} - \arctan \frac{\dot{z}_e}{\dot{x}_e} \tag{22}$$

$$F_e = \rho S_e \sin\alpha_e(\dot{z}_e^2 + \dot{x}_e^2) \tag{23}$$

$$\phi_k = \phi_{k-1} + k_s(u_k - \phi_{k-1})\Delta t \tag{24}$$

$$\dot{x}_k = (-\frac{F_w \sin\theta_{k-1} + F_e \sin\theta_{k-1} + \phi_{k-1}}{m})\Delta t + \dot{x}_{k-1} \tag{25}$$

$$\dot{z}_k = (\frac{F_w \cos(\theta)_{k-1} + F_e \cos\theta_{k-1} + \phi_{k-1}}{m} - g)\Delta t + \dot{z}_{k-1} \tag{26}$$

$$\dot{\theta}_k = (\frac{F_w * l_w - F_e(l\cos\phi_{k-1} + l_e)}{I})\Delta t + \dot{\theta}_{k-1} \tag{27}$$

$$x_k = x_{k-1} + \dot{x}_k\Delta t \tag{28}$$

$$z_k = z_{k-1} + \dot{z}_k\Delta t \tag{29}$$

$$\theta_k = \theta_{k-1} + \dot{\theta}_k\Delta t \tag{30}$$

The measurement equations are:

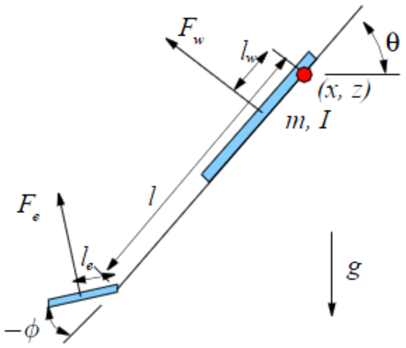

Figure 14. Glider Model

$$B_z = -\frac{\mu_0 I_c (x-d)}{2\pi((x-d)^2+z^2)} + \frac{\mu_0 I_c (x+d)}{2\pi((x+d)^2+z^2)} \tag{31}$$

$$B_x = \frac{\mu_0 I_c z}{2\pi((x-d)^2+z^2)} - \frac{\mu_0 I_c z}{2\pi((x+d)^2+z^2)} \tag{32}$$

The measurement equations are actually a function of θ due to the required coordinate transform from the world coordinates to the glider's coordinate system.

$$B_{x_{glider}} = B_x cos(\theta) - B_z sin(\theta) \tag{33}$$

$$B_{z_{glider}} = B_x sin(\theta) + B_z cos(\theta) \tag{34}$$

The above model is then used to propagate forward a specified number of particles, each one acting like an individual glider. To each new particle state estimate, Gaussian noise is added, which is equivalent to sampling the predicted states from some Gaussian distribution. Once all the particles have been propagated forward, the position measurements are incorporated and the particle weights are determined.

It can be easily reasoned that a probability distribution could be represented, as shown in the equation below, as a large set of points with specified weights.

$$p(x) = \sum_{i=1}^{N_s} w^i \delta(x - x^i) \tag{35}$$

Thus the weights on those particles can be updated recursively by the equation:

$$w_k^i = w_{k-1} p(z_k | x_{k-1}) \tag{36}$$

$$w_k = \frac{w_k}{\displaystyle\sum_{i=1}^{N_s} w^i} \tag{37}$$

It is important to remember that the weights must be normalized in order to represent a true probabilistic distribution.

To incorporate the position measurements for the glider position estimation, the weights are computed as a collection of Gaussian functions at the probable points $p(z_k|x_{k-1})$, if position is assumed to be your measurement.

The Gaussian functions are defined as follows:

Measurement Error Vector **y**:

$$\begin{pmatrix} (x_{measurement} - x_k^i) & (z_{measurement} - z_k^i) & (\theta_{measurement} - \theta_k^i) & (\dot{\theta}_{measurement} - \dot{\theta}_k^i) \end{pmatrix}$$

Covariance Matrix **C**:

$$\begin{pmatrix} C_1 & 0 & 0 & 0 \\ 0 & C_2 & 0 & 0 \\ 0 & 0 & C_3 & 0 \\ 0 & 0 & 0 & C_4 \end{pmatrix}$$

Gaussian Function:

$$\frac{1}{\sigma\sqrt{2\pi}} e^{\left(-\frac{\mathbf{y}\mathbf{C}\mathbf{y}^T}{2\sigma^2}\right)} \tag{38}$$

Before being carried out on the actual, instrumented aircraft, the representative data was created to evaluate the particle filtering algorithm in simulation. The dynamics of the aircraft were simulated in the presence of a simulated magnetic field, and then the magnetic field measurements were modulated, demodulated, and subjected to noise. Below are the successful simulation results of the particle filter, where $N_s = 400$

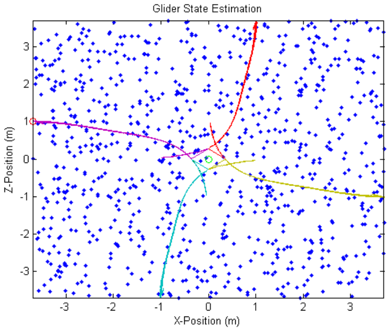

Figure 15. Particle Filter Simulation Execution: Frame 1

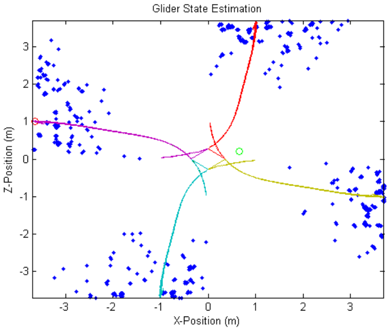

Figure 16. Particle Filter Simulation Execution: Frame 2

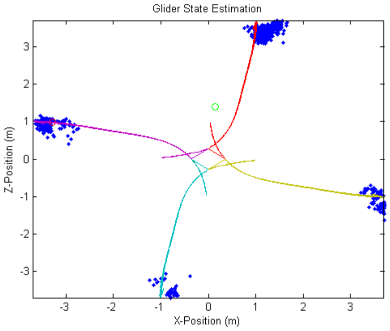

Figure 17. Particle Filter Simulation Execution: Frame 3

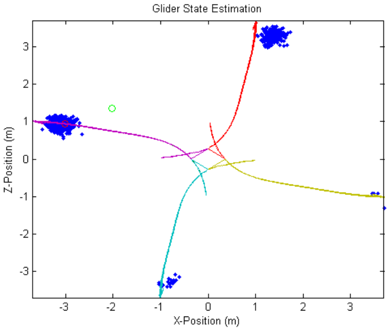

Figure 18. Particle Filter Simulation Execution: Frame 4

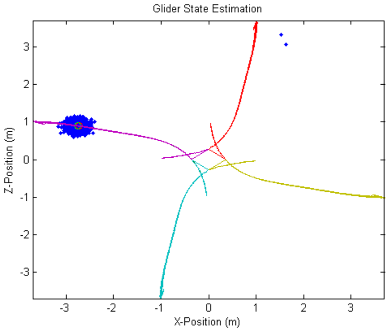

Figure 19. Particle Filter Simulation Execution: Frame 5

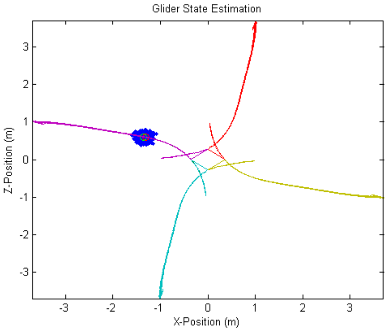

Figure 20. Particle Filter Simulation Execution: Frame 6

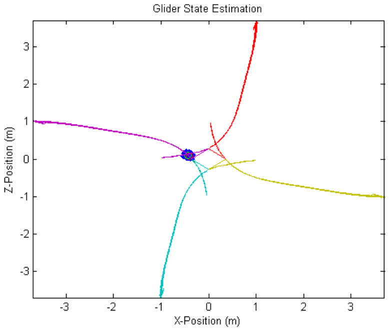

Figure 21. Particle Filter Simulation Execution: Frame 7

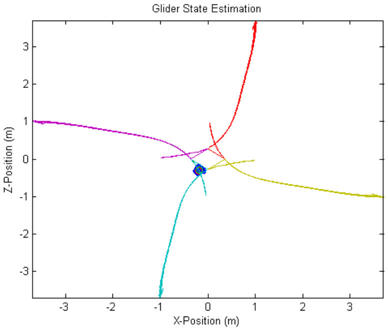

Figure 22. Particle Filter Simulation Execution: Frame 8

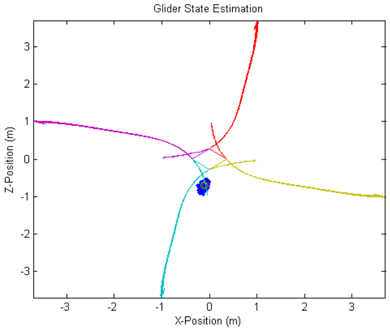

Figure 23. Particle Filter Simulation Execution: Frame 9

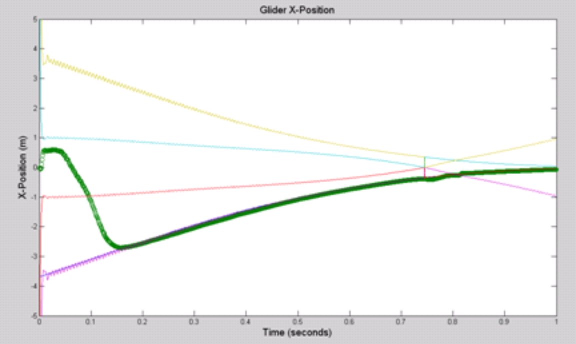

Figure 24. Particle Filter Simulation X-position Estimation

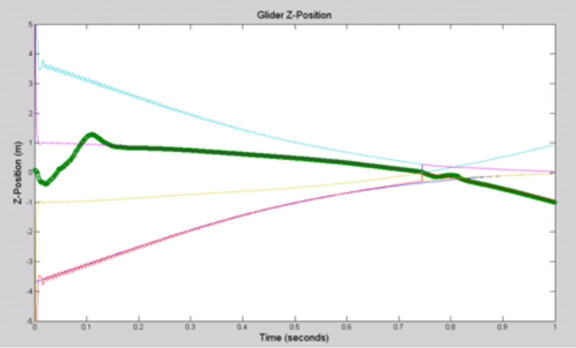

Figure 25. Particle Filter Simulation Z-position Estimation

XI. Discussion

In addition to being a significant step forward in the effort to use powerlines for UAV power harvesting, the investigations outlined in this paper have also demonstrated the incredible power of the particle filter in its ability to solve extraordinarily difficult state estimation problems. Even now, the full potential of the particle filter is not being used. One could imagine vastly improving the measurement system by using the particle filter to take into account zero crossings in the demodulated data. In this way, the particle filter could almost become a means of estimating a discrete state by using measurement conditions or events to adjust weights in the probability density. This notion also melds nicely with the nature of the magnetic field, which increases in magnitude quadratically as the distance decreases By using the particle filter's versatile information fusion capabilities, measurements closer to the powerline might be able to be trusted more in the measurement update since the signal to noise ration increases so dramatically as one moves toward the wire. In an era where computational resources are becoming less and less costly, it is important to remember that powerful tools which have been developed by computer scientists in the past and were once too intractable do to their required computational resources, can now be used to solve some the most difficult problems in estimation and control.

XII. Conclusions

The initial attempts at localizing a fixed wing aircraft using the magnetic field surrounding a powerline has demonstrated promising results. Furthermore, all the algorithms used have been causal and will transfer directly to an microprocessor operating in real-time. Not only does this robotic vision method open up a range of practical applications for UAV perching maneuvers, but it will also allow for outdoor experimentation in the near future. Now that the particle filter is working in simulation, the next step is to acquire acceptable data from on-board the glider during a flight maneuver, and then to process that data using the particle filtering algorithms. Because we have access to advanced motion capture equipment, it will be an extraordinarily simple task to evaluate the performance of the estimation algorithm. Then, once the algorithm proves to be successful in handling the real data, the particle filter and accompanying algorithms will be transferred over to an embedded unit to run in real-time.

Acknowledgments

The authors would like to thank Warren Hoburg for his help with glider manufacturing, Jim Hoburg for his help with magnetic field analysis. This work was funded by a contract with the Defense Research Associates, Inc in collaboration with the AFRL PLUS program.

References

[1] Cory, R. and Tedrake, R., "Experiments in Fixed-Wing UAV Perching," *Proceedings of the AIAA Guidance, Navigation, and Control Conference*, AIAA, 2008.

[2] Hoburg, W., Roberts, J. W., Moore, J., and Tedrake, R., "The Perching Number: A Dimensionless Analysis of Post-stall Maneuvering in Birds and Planes," *Working Draft*, 2009.

[3] Wickenheiser, A. M. and Garcia, E., "Longitudinal Dynamics of a Perching Aircraft," *Journal of Aircraft*, Vol. 43, No. 5, 2006, pp. 1386–1392.

[4] Wickenheiser, A. M. and Garcia, E., "Optimization of Perching Maneuvers Through Vehicle Morphing," *Journal of Guidance, Control, and Dynamics*, Vol. 31, No. 4, July-August 2008, pp. 815–824.

[5] Sigurd, K. and How, J., "UAV trajectory design using total eld collision avoidance," *AIAA Guidance, Navigation, and Control Conference and Exhibit*, August 11-14 2003.

[6] Chavanne, B., "Small UAV's may Recharge on Powerlines," 2007.

[7] Roberts, J. W., Cory, R., and Tedrake, R., "On the Controllability of Fixed-Wing Perching," *Accepted in the Proceedings of the American Controls Conference (ACC)*, 2009.

[8] Hoburg, W. and Tedrake, R., "System Identification of Post Stall Aerodynamics for UAV Perching," *AIAA Infotech@Aerospace Conference, Seattle, WA*, March 2009.

[9] Thrun, S., Burgard, W., and Fox, D., *Probabilistic Robotics*, MIT Press, 2005.

[10] Dellaert, F., Fox, D., Burgard, W., and Thrun, S., "Monte Carlo Localization for Mobile Robots," *Proceedings of the IEEE International Conference on Robotics and Automation*, 1999.

[11] Rekleitis, I., "A Tutorial for Mobile Robot Localization," *Proceedings of the IEEE International Conference on Robotics and Automation*, 2003.

[12] Noll, Nishimura, D., Macovski, D., and A., "Homodyne detection in magnetic resonance imaging," *Medical Imaging, IEEE Transactions on*, Vol. 10, No. 2, 1991, pp. 154–163.

[13] Arulampalam, S., Maskell, S., Gordon, N., and Clapp, T., "A Tutorial on Particle Filters for On-line Non-linear/Non-Gaussian Bayesian Tracking," *IEEE Transactions on Signal Processing*, Vol. 50, No. 2, feb 2002, pp. 174–188.

[14] Carmi, A., "Adaptive Particle Filtering for Spacecraft Attitude Estimation from Vector Observations," *Journal of Guidance, Control, and Dynamics*, Vol. 32, No. 1, 2009, pp. 232–241.

[15] Lenz, J. and Edelstein, S., "Magnetic sensors and their applications," *Sensors Journal*, Vol. 6, No. 3, June 2006, pp. 631–649.

[16] Oppenheim, A., Willsky, A., and Hamid, S., *Signals and Systems*, Prentice Hall, 2nd ed., August 1996.

[17] Rouger, P., "Guidance and Control of Artillery Projectiles with Magnetic Sensors," *Proceedings of the 45th AIAA Aerospace Sciences Meeting and Exhibit*, AIAA, January 8-11 2007.

[18] Kingston, D. B. and Beard, R. W., "Real-Time Attitude and Position Estimation for Small UAVs Using Low-Cost Sensors," *Proceedings of the AIAA 3rd Unmanned Unlimited Systems Conference and Workshop*, AIAA, September 20-23 2004.

[19] Marins, J., Yun, X., Bachmann, E., McGhee, R., and Zyda, M., "An extended Kalman filter for quaternion-based orientation estimation using MARG sensors," *Proceedings of the IEEE/RSJ International Conference on Intelligent Robots and Systems*, 2001, pp. 2003–2011.

[20] Lenz, J., "A review of magnetic sensors," *Proceedings of the IEEE*, Vol. 78, No. 6, June 1990, pp. 973–989.

[21] Yassa, Noujaim, F., and S.E., "Adaptive Synchronous Amplitude Demodulation," *Signals, Systems and Computers*, Vol. 1, 1988, pp. 107–111.

[22] Yabukami, Kikuchi, S., Yamaguchi, H., Arai, M., K.I.Takahashi, Itagaki, K., Wako, A., and N., "Motion capture system of magnetic markers using three-axial magnetic field sensor," *agnetics, IEEE Transactions on*, Vol. 36, No. 5, September 2000, pp. 3646–3648.